Journal of Agricultural Sciences
(Tarim Bilimleri Dergisi)

J Agr Sci-Tarim Bili
e-ISSN: 2148-9297
jas.ankara.edu.tr

Evaluation of Classification Accuracy of Spectral Indices and Machine Learning Algorithms for Greenhouse Detection Using the Google Earth Engine Platform

Ramazan Gungor[a*], Fusun Balik Sanli[b], Ali Murat Ates[c], Osman Salih Yilmaz[a]

[a] *Demirci Vocational School, Manisa Celal Bayar University, 45900, TURKEY*

[b] *Geomatic Engineering Department, Yildiz Technical University, 34220, TURKEY*

[c] *Computer and Instructional Technologies Department, Faculty of Education, Manisa Celal Bayar University 45900, TURKEY*

ARTICLE INFO
Research Article
Corresponding Author: Ramazan Gungor, E-mail: ramazan.gungor@cbu.edu.tr
Received: 27 June 2024 / Revised: 25 August 2025 / Accepted: 20 September 2025 / Online: 20 January 2026

Cite this article
Gungor R, Sanli F B, Ates A M, Yilmaz O S (2026). Evaluation of Classification Accuracy of Spectral Indices and Machine Learning Algorithms for Greenhouse Detection Using the Google Earth Engine Platform. *Journal of Agricultural Sciences (Tarim Bilimleri Dergisi),* 32(1):158-176. DOI: 10.15832/ankutbd.1728949

ABSTRACT
Accurate mapping of greenhouse areas is critically important for enhancing agricultural productivity and mitigating environmental impacts. Recently, remote sensing technologies have emerged as powerful tools for detailed and accurate detection of greenhouse areas and land use. The main objective of the study, which is to evaluate the effectiveness of spectral indices and Machine Learning (ML) algorithms in detecting greenhouse areas. This study employs Random Forest (RF), Support Vector Machine (SVM), and Classification and Regression Trees (CART) ML algorithms to classify Harmonized Sentinel-2 MSI (Multispectral Instrument) satellite imagery using the Google Earth Engine (GEE) platform. In addition, indices such as the Normalized Difference Vegetation Index (NDVI), Plastic Greenhouse Index (PGI), Retrogressive Plastic Greenhouse Index (RPGI), Plastic Mulched Landcover Index (PMLI), and Greenhouse Vegetable Land Extraction Index (Vi) were calculated and incorporated as bands for classification. In the study, a total of 7 data sets were created using various ML algorithms and indices. The highest overall accuracy (OA) and kappa (*K*) values were obtained as 88.10% and 0.804, respectively, in the classification using the PGI and RF algorithm. To test the significance of the accuracy assessment, the McNemar test was applied. The most significant relationship was observed in comparisons using the PGI and RF classifier, where the calculated statistic was greater than the critical χ^2value (χ^2=3.84 at 95% confidence interval).

Keywords: Antalya, GEE, Greenhouse, Machine Learning Algorithm, PGI

1. Introduction

The steadily increasing global population and finite land resources highlight the importance of efficient land use and land cover management, making the accurate mapping and registration of land use purposes critically important in this context. Land Use/Land Cover (LULC) classification provides valuable insights for monitoring and managing land use patterns, offering practical solutions to challenges posed by urbanization, global warming, and climate change in terms of resource management, planning, and environmental conservation (Ayazli 2024; Z. Zhao et al. 2024). A primary focus in addressing these challenges lies in accurately classifying land into broad categories and producing precise LULC maps. Accurately classified LULC data can contribute to a wide range of studies at various scales and regions (Avtar et al. 2019; Qu & Long 2018; Stehfest et al. 2019). One crucial area of application is agricultural land, which is at the heart of addressing the global food crisis. Keeping records of agricultural lands up-to-date is essential for informed land management decisions (McBratney et al. 2014). In this context, information regarding greenhouse areas is crucial for enhancing agricultural productivity, planning land use, and assessing the impacts on ecosystems. Nowadays, remote sensing (RS) techniques are highly effective and practical for obtaining such information, generating LULC maps, and monitoring land use types. Modern RS sensors provide highly precise data across different resolution levels. Satellite imagery obtained from various platforms offers low-resolution (Moderate Resolution Imaging Spectroradiometer, MODIS), medium-resolution (Landsat), and high-resolution (WorldView, Sentinel) data (Drusch et al. 2012). These images provide not only spatial resolution but also rich information in terms of spectral, radiometric, and temporal resolution (Dou et al. 2021; Mary et al. 2023; Tariq et al. 2023). However, due to the high costs associated with acquiring high-resolution data, their application in generating land-related information is often limited (Malarvizhi et al. 2016; Stoian et al. 2019). Instead, lower-cost or free images from satellite platforms such as Landsat or Sentinel-2 MSI (Multispectral Instrument) are commonly preferred (Al-Najjar et al. 2019; Zhu et al. 2021).

LULC maps generated using RS techniques with satellite imagery play a crucial role in identifying greenhouse areas, which is important for agricultural activities and sustainability (Castaldi et al. 2016; Dematte et al. 2018). Plastic-covered greenhouses exhibit relatively higher reflectance values across the electromagnetic spectrum compared to other land cover types (Yang et al. 2017). Consequently, greenhouse areas can be accurately detected in medium-resolution satellite imagery (Aguilar et al. 2015; González-Yebra et al. 2018; Jiménez-Lao et al. 2020; Nemmaoui et al. 2018; Novelli et al. 2016; Ou et al. 2020; Yang et al. 2017). Image processing techniques such as object-based or pixel-based classification, along with indices derived from arithmetic band combinations, can be employed for greenhouse mapping, depending on the quality of the data used (Yang et al. 2017). In recent studies on land classification, machine learning (ML) algorithms such as Maximum Likelihood (MLi), Decision Trees (DT), Classification and Regression Trees (CART), Random Forest (RF) and Support Vector Machines (SVM) are frequently used in the detection of greenhouse areas.

A series of indices have also been developed to mathematically analyse spectral reflectance at different wavelengths to detect greenhouse areas from satellite images. Zhao GengXing et al. (2004) conducted a systematic analysis of spectral characteristics of different land use types to develop a rapid and accurate method for extracting greenhouse land information, resulting in the Greenhouse Vegetable Land Extraction Index (Vi) which utilizes SWIR1, NIR, and R bands. Salas & Henebry (2012) introduced the Moment Distance Index (MDI) to measure the similarity between two or more spectral images. Lu et al. (2014) developed the Plastic Mulched Landcover Index (PMLI) to differentiate greenhouse areas from other land cover types using SWIR1 and Red (R) bands. Aguilar et al. (2016) first applied MDI to greenhouse detection and developed the Greenhouse Detection Index (GDI) using Blue (B), SWIR1, and Short-Wave Infrared 2 (SWIR2) bands. The Plastic Greenhouse Index (PGI), developed by (Yang et al. 2016) in the same years, has demonstrated significant success in detecting plastic-covered areas. This index is calculated using visible (RGB), Near-Infrared (NIR), and Short-Wave Infrared 1 (SWIR1) bands. Yang et al. (2017) developed the Retrogressive Plastic Greenhouse Index (RPGI) to improve the accuracy of PGI. Ibrahim & Gobin (2021) used this index with Sentinel-2 data to differentiate and map greenhouse areas from soil and vegetation.

Studies conducted to generate LULC maps typically cover large areas and require comprehensive analysis of numerous satellite images. The workstations used for these analyses demand significant storage and processing capabilities. However, recent advancements in cloud computing have enabled users to perform analyses online through cloud platforms without the need for any software (Gorelick et al. 2017). One of these platforms is Google Earth Engine (GEE), which hosts an enormous collection of satellite imagery (Yilmaz et al. 2023). This platform is designed to facilitate rapid production of various time series analyses, future projections, and mapping techniques (Goldblatt et al. 2016). Moreover, GEE provides access to petabytes of data and enables analysis through its Application Programming Interface (API) using JavaScript and Python (Patela et al. 2015).

The novelty of this study lies in the comparative evaluation of five different spectral band indices—both individually and in various combinations—using three distinct machine learning algorithms for greenhouse detection within the boundaries of Antalya Province, and in the systematic analysis of the impact of the selected indices on classification accuracy.

While there are existing studies in the literature focusing on the identification and mapping of greenhouse areas using RS techniques, comprehensive investigations integrating such a wide range of ML algorithms and spectral indices at this scale are rather limited. Furthermore, the utilization of a high-performance computing platform like GEE significantly enhances the reproducibility and scalability of the analyses, thereby contributing meaningfully to the scientific literature. Accordingly, the primary objective of this study is to identify the most effective combination of ML algorithm and spectral index that enables the production of highly accurate greenhouse maps. In addition to this main goal, the following specific objectives are set:

I. To examine the impact of different spectral indices on classification performance using Sentinel-2 satellite imagery within the GEE platform.

II. To compare the classification performance of RF, SVM, and CART ML algorithms.

III. To reveal the statistical differences among classifications through the McNemar test.

IV. To develop the most successful model and analyze the accuracy metrics of its attributes.

V. This study provides a comprehensive guide for selecting the most appropriate algorithms and indices to detect greenhouses in different geographical regions using RS techniques. The research aims to accelerate the integration of technology in this field by providing in-depth information on how RS technology can be strategically applied in the agricultural sector.

RS imagery, with its diverse spatial and spectral resolutions, provides a great data source for the temporal monitoring and mapping of greenhouse areas. Traditional techniques for the detection and monitoring of greenhouse areas are often costly and time-consuming. Therefore, in addition to object-based and pixel-based classification methods, indices derived from the spectral properties of images are widely used in greenhouse classification. However, studies combining GEE, ML algorithms, and band indices in this field are limited (Gao et al. 2022; Ou et al. 2020). However, studies that integrate ML algorithms with cloud-based

geospatial analysis platforms such as GEE have yielded promising results. Ou et al. (2020) investigated the temporal changes in greenhouse areas within protected agricultural lands from 1990 to 2018 by utilizing Landsat satellite imagery and the GEE platform. To enhance classification accuracy, they analyzed and ranked the importance of spectral, index-based, and texture-based features. Within this scope, LULC classification was performed using the RF ML algorithm. The classification results yielded a user's accuracy (UA) of 96%, a producer's accuracy (PA) of 86%, an F1-Score (F1-S) of 0.91, and an overall accuracy (OA) exceeding 90%. Furthermore, indices such as the Normalized Difference Tillage Index (NDTI) and the PGI were identified as playing a critical role in greenhouse detection. The study also highlighted that the SLC-off issue present in Landsat 7 ETM+ imagery, along with cloud cover, adversely affected the consistency of the classification maps. However, the proposed Probability-based Temporal Consistency Correction (PTCC) algorithm successfully mitigated inconsistencies between classifications, improving classification accuracy by an average of 5% and alleviating the impact of the SLC-off problem.

Gao et al. (2022) conducted a study on the GEE platform to evaluate the performance of various ML algorithms for the detection of greenhouse areas. In this context, they employed the Minimum Distance Classifier (MDC), Support Vector Machine (SVM), CART, and RF algorithms. All algorithms achieved OA values exceeding 84%, with the highest classification accuracy of 94% obtained using the SVM algorithm. Among the methods tested, the MDC algorithm produced the least accurate results. The calculated greenhouse area increased from 5.92 km² in 2000 to 194.42 km² in 2019, with the most significant expansion occurring between 2010 and 2015. However, the study identified certain limitations, such as the inability to distinguish greenhouse areas on satellite imagery during the 1990–1995 period due to their extremely small size, and the use of only 25% of the available samples in the logistic regression analysis. Xiong et al. (2019) investigated the potential of the GEE cloud computing platform for greenhouse detection using multi-sensor and multi-temporal satellite imagery, including Sentinel-2 MSI, Landsat 5–8, and MODIS. The study employed the CART ML algorithm. According to the results, the F1-S for greenhouse areas was reported as 0.91, with an OA of 92%, a PA of 97%, and a UA exceeding 86%. Perilla & Mas (2019) aimed to map greenhouse areas using high-spatial resolution Sentinel-2 MSI satellite imagery in conjunction with the GEE platform. The study employed the Maximum Entropy classifier. To enhance classification accuracy, several spectral indices—NDVI, Normalized Difference Water Index (NDWI), Green Normalized Difference Vegetation Index (gNDVI), PGI, Plastic Mulch Land Index (PMLI), and Normalized Difference Built-up Index (NDBI)—were incorporated into the imagery. The classification results yielded an OA exceeding 70%. Additionally, the blue (B), NIR, SWIR1, SWIR2 bands were identified as the most effective in distinguishing greenhouse areas from other land cover types due to their superior spectral separability. Zhang et al. (2022) performed greenhouse area classification on the GEE platform using Sentinel-1 and Sentinel-2 datasets. The study incorporated index-based, spectral, texture, and PCA-MR (Principal Component Analysis of Multi-Source Remote Sensing Data) features. The RF algorithm was selected for classification, with the number of decision trees set to 100. A total of 11 classification scenarios were generated based on different combinations of input features. The inclusion of PCA-MR features resulted in the highest OA, reaching 93%. However, the presence of fragmented and small-scale agricultural plots introduced mixed pixel challenges, and the contribution of Sentinel-2 texture features to classification accuracy was found to be limited. Veettil & Xuan (2022) employed an unsupervised classification method—K-Means clustering—for the detection of greenhouse areas using Landsat-8 OLI and Sentinel-2 MSI satellite imagery. The study utilized the mean values of NDVI, PGI, Refined Plastic Greenhouse Index (RPGI), and NDBI to support the classification process. The OA for greenhouse classes generated from spectral indices derived from Sentinel-2 MSI and Landsat-8 imagery was calculated as 91% and 89%, respectively. For the K-Means classification, the estimated OA were 73% and 72%, respectively. Moreover, the inclusion of PGI in the classification process reduced the misclassification rate of urban areas as greenhouses. Nonetheless, the study faced several limitations, including a lack of optical data and spectral confusion between greenhouses, other plastic-covered surfaces, and urban areas. Z. Zhao et al. (2024) conducted a study on the GEE platform using Sentinel-2 MSI imagery to generate classification maps for various land cover types and to evaluate the classification performance of RF, SVM, and CART ML algorithms. Additionally, NDVI, NDBI, and the Modified Normalized Difference Water Index (MNDWI) were incorporated as supplementary bands in the classification process. Based on the computed metrics, the RF classifier outperformed both SVM and CART in terms of accuracy. The Kappa (***K***) coefficients for CART, SVM, and RF were reported as 0.94, 0.95, and 0.97, respectively, while the corresponding average OA were calculated as 96%, 97%, and 98%. However, the study was constrained by limitations such as high cloud cover and the absence of optical data during certain time intervals, as well as spectral confusion between bare land and urban areas.

2. Material and Methods

Antalya Province is in southwestern Turkey, between longitudes 29° 20' - 32° 35' East and latitudes 36° 07' - 37° 29' North. Antalya, the westernmost province of the Mediterranean Region, is surrounded by the Taurus Mountains to the north and east, and the Mediterranean to the south. The northern position of the Taurus Mountains, proximity to the Mediterranean Sea, and the regional river systems constitute natural factors that distinguish Antalya in terms of agricultural production and greenhouse activities (Figure 1). The province, which constitutes 17.6% of the total area of the region, has a rich natural and cultural geography. Antalya covers an area of 20,587.438 km², representing 2.6% of Turkey's total area (Koc-San et al. 2013). Offering significant ecological suitability and agricultural potential together with the Antalya Plain, the province is an important region for Turkish agriculture. Consequently, one-fifth of Antalya's land is dedicated to agriculture. Greenhouse farming is one of the most important agricultural activities in the region. According to the Turkish Statistical Institute (TUIK) data, the total area of greenhouses in Antalya has steadily increased in recent years, reaching 854,600 decares of various types of greenhouses by 2021 (https://data.tuik.gov.tr/Kategori/GetKategori?p=Tarim-111). This area accounts for 83% of Türkiye's glasshouse area and 51%

of its plastic greenhouse area (Koc-San 2013). Antalya province was selected as the investigation area in this study. The presence of different types of greenhouse areas with high spectral variability within the selected area makes it suitable for investigating the contribution of ML algorithms and band indices to classification accuracy within the scope of this study.



Figure 1- Study area

The study comprises four main processing stages. In the first stage, the image collection created on the GEE platform underwent pre-processing, involving the application of a 5% cloud mask and cropping to the study area. In addition, pixel values were subjected to mosaic processing and median statistics to reduce image clutter caused by multiple images and obtain a single image. 6 distinct LULC classes were established: urban, water, bare land, vegetation, agriculture, and greenhouse based on the pre-processed image and considering the region's land characteristics. During the sampling process, a stratified random sampling method was applied based on the spatial characteristics of each class, resulting in a total of 2450 sample points being collected. The stratified random sampling method is a statistical sampling technique employed to obtain balanced and objective samples from datasets comprising heterogeneous classes (Phinzi et al. 2023; Sun et al. 2025). In the second stage, pixel-based supervised classification methods were applied to distinguish greenhouse areas from other land cover classes. The classification process was carried out on the GEE platform by writing JavaScript code. At this stage, a total of seven different datasets were created using the RGB and NIR bands of Sentinel-2 MSI satellite imagery, along with NDVI, PGI, RPGI, PMLI, Vi, and MultiIndex (Table 1). Then, separate classification processes were performed for each dataset and algorithm to determine their impact on classification accuracy. The selection of the RF, SVM, and CART ML algorithms for the classification stage was informed by their widespread adoption in RS classification studies and their proven effectiveness in delivering robust results. In particular, the RF algorithm's resilience to overfitting, the inherently interpretable structure of the CART algorithm, and the SVM algorithm's strong performance in high-dimensional datasets collectively render these three ML algorithms well-suited for comparative analyses. In the third phase, a total of 2,000 points were selected from the classified image and validated using high-resolution satellite imagery available on the Google Earth platform. This method is widely employed in the literature for accuracy assessment due to the temporal coverage and global accessibility of Google Earth imagery. The reference images used on the Google Earth platform are primarily derived from commercial satellites operated by Maxar Technologies (e.g., WorldView 1–4 and GeoEye-1), which provide sub-meter spatial resolution in most regions (Manos et al. 2022). The Google Earth image dates were chosen to be close to the satellite image dates to ensure the reliability of the accuracy test. The accuracy of the classification was determined by calculating the OA, *K*, Recall (Rc), Precision (Pr), F1-S, Specificity (Spc), and Accuracy (Ac) metrics. In the fourth stage of the application, boundary cleaning and majority filtering cartographic generalization processes were applied to the classified image with the highest accuracy. These procedures were performed using ArcGIS Pro 3.2 software to correct misclassified single pixels. Afterwards, the generalized raster data was converted into vector format, and the areas of the classes were calculated. The workflow of the study is given in Figure 2.

Table 1- Datasets in the current study

Dataset ID	*Datasets*
DS1	RGB+NIR
DS2	RGB+NIR+NDVI
DS3	RGB+NIR+PGI
DS4	RGB+NIR+RPGI
DS5	RGB+NIR+PMLI
DS6	RGB+NIR+V_i
DS7	RGB+NIR+NDVI+PGI+RPGI+PMLI+V_i

The datasets presented in Table 1 constitute a fundamental framework for evaluating the classification performance of this study. Among these, DS1—comprising only RGB and NIR bands—was adopted as the starting point of the analysis. These core bands are widely employed in greenhouse detection studies and were selected to establish the baseline performance of the classification algorithms. In datasets DS2–DS6, various spectral indices were integrated in addition to the conventional bands. The purpose of this integration was to assess the extent to which each index could discriminate greenhouse areas from other land cover classes. Consequently, the contribution of individual indices to classification accuracy was comparatively analyzed. DS7, on the other hand, represents a comprehensive combination in which all spectral indices used in the study are employed alongside the conventional bands. This dataset was designed to evaluate the impact of multi-index integration on classification performance, as compared to the best-performing single-index dataset.

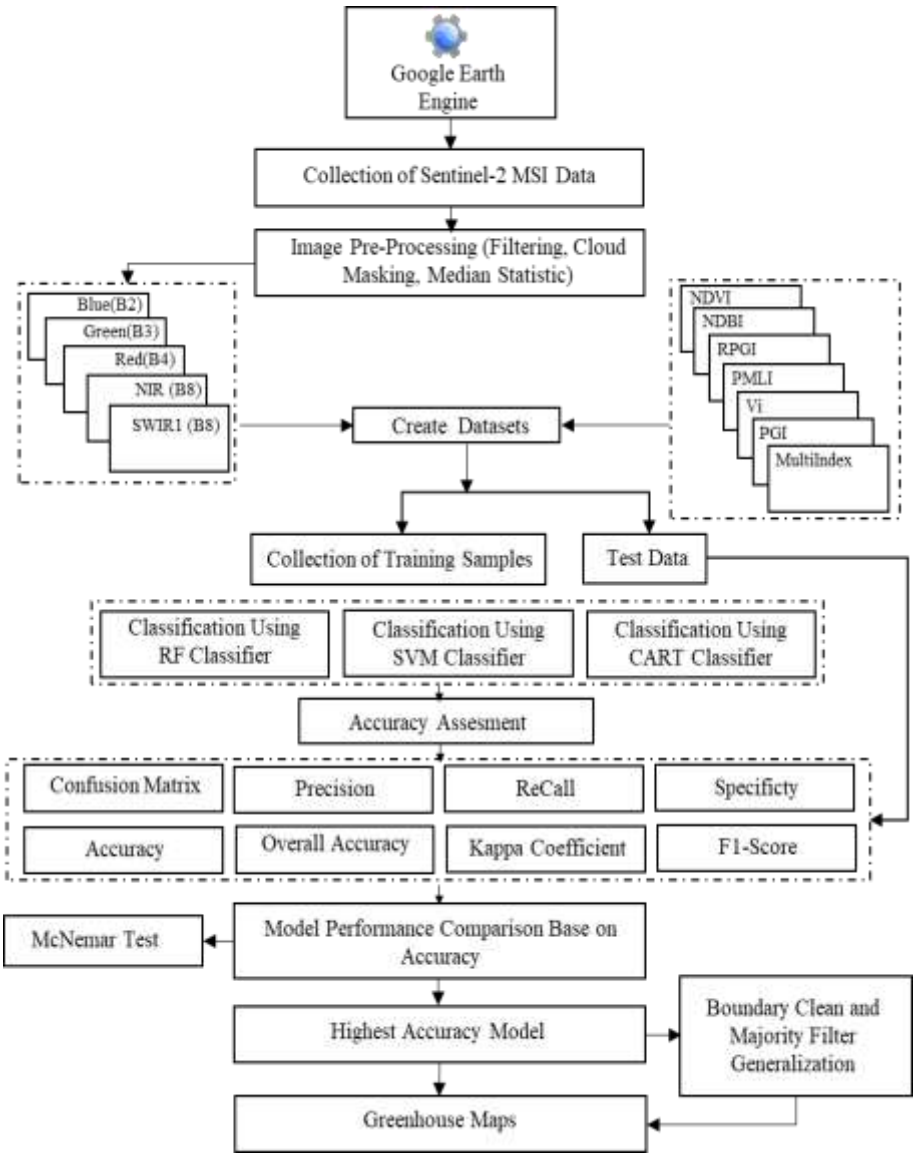

Figure 2- Workflow of the study

2.1. Satellite data

In the present study, Harmonized Sentinel-2 MSI satellite imagery, accessed via the GEE platform, was utilized to map the selected land cover classes. These images are derived from the Sentinel-2A and Sentinel-2B satellites and have undergone atmospheric correction using the Sen2Cor algorithm to generate bottom-of-atmosphere (BOA) reflectance values. Data from both satellites were integrated into a single harmonized collection, ensuring spectral consistency through band alignment, radiometric calibration, and metadata standardization (Gröschler et al. 2025). The Harmonized Sentinel-2 MSI dataset comprises four spectral bands at 10 m spatial resolution, six bands at 20 m, and three bands at 60 m (Djamai & Fernandes 2018; Drusch et al. 2012). The satellite imagery used in this study was accessed through the Copernicus Open Access Hub (https://scihub.copernicus.eu/) via the GEE platform. Imagery was selected within the date range of July 7, 2023, to August 15, 2023, and filtered using a 5% cloud mask. A total of 107 images were aggregated using the median statistic. Additionally, to ensure consistency in spatial resolution across all bands used in the study, the SWIR1 band was resampled to a spatial resolution of 10 meters using the bilinear interpolation method. The spectral characteristics of the Harmonized Sentinel-2 MSI bands are presented in Table 2.

Table 2- Specification of Harmonized Sentinel-2 MSI spectral bands applied in the image classifications

Bands	*Central Wavelength (S2A/S2B) (μm)*	*Band Width (S2A/S2B) (μm)*	*Spatial Resolution (m)*
Blue (B2)	0.496	0.060	10
Green (B3)	0.560	0.036	10
Red(B4)	0.664	0.031	10
NIR (B8)	0.835	0.106	10
SWIR1 (B11)	1.610	0.091	20
Harmonized Sentinel-2 MSI, Level-2A (July-August2023)			

2.2. Various spectral indexes used for mapping Greenhouse Cover

Spectral indices are derived from the combination of reflection values at two or more wavelengths from any object or land surface. These spectral index values have been utilized in numerous studies for the detection of greenhouse areas (Aguilar et al. 2021; Ibrahim & Gobin 2021; Novelli & Tarantino 2015; Veettil & Xuan 2022). In the present study, the NDVI, PGI, RPGI, PMLI, and V_i indices were used (Table 3). Rouse et al. (1974) proposed the NDVI to monitor vegetation across different phenological periods and spectral reflectance ranges. NDVI is an index used to determine the density and health of vegetation. This index utilizes the difference between NIR and R reflectance to measure the photosynthetic capacity of vegetation (Mallick et al. 2024). The energy reflected by different plant species and parts can vary slightly due to differences in plant physical structure, form, chlorophyll pigment, and environment. Therefore, NDVI values typically range from -1 to +1 (Veettil et al. 2022). Higher NDVI values indicate denser and healthier vegetation, while lower values indicate reduced or unhealthy vegetation. NDVI has been successfully applied in greenhouse detection studies due to its ability to produce strong contrast between vegetated and non-vegetated surfaces, and it is calculated as shown in Equation 1 (Xue & Su 2017). Another index used in the detection of greenhouse surface areas is the PGI. This index, developed by (Yang et al. 2017), is calculated as the average of RGB, NIR, and SWIR1 bands. PGI uses threshold values to distinguish greenhouse areas from man-made features and vegetation. It suggests that pixel values greater than 0.73 should be considered non-greenhouse areas for vegetation, and pixel values greater than 0.005 should be considered non-greenhouse areas for man-made features. The PGI value is calculated as shown in Equation 2. Yang et al. (2017) enhanced the variance of the PGI by focusing on plant growth under greenhouses and developed the RPGI by removing the ($\rho_{NIR} - \rho_{Red}$) factor from the PGI formula. The RPGI value is calculated as shown in Equation 3. Since PGI and RPGI exploit the spectral differences between the red and NIR bands, they are influenced differently by vegetation and plastic-covered greenhouse materials. This spectral divergence provides a distinct advantage in accurately identifying greenhouse areas. The R band experiences significant absorption by chlorophyll resulting in low reflectance values in areas with dense vegetation. However, it exhibits high reflectance values in bare soil surfaces with little or no vegetation (Maccioni et al. 2001). Consequently, there is little difference in reflectance values among greenhouse-covered areas, regions with early-growing plants, newly ploughed fields, and areas with sparse vegetation. On the other hand, the SWIR1 band shows high absorption in water bodies and water-saturated soil areas, while demonstrating high reflectance in saline or dry soil surfaces (Mokhtari et al. 2023). Since the surface water content of greenhouse areas and open fields does not differ significantly, their reflectance in the SWIR1 band is also expected to be similar. Lu et al. (2014) proposed the PMLI for mapping greenhouse areas using the reflectance values of these two bands and calculated it as shown in Equation 4. V_i, proposed by (Zhao GengXing et al. 2004), is an index developed for rapid mapping of greenhouse-covered areas. By utilizing the spectral differences between various land cover classes and employing the R, NIR, and SWIR1 bands, V_i aims to identify areas with high reflectance, corresponding to greenhouse areas. To this end, the V_i value is calculated as presented in Equation 5.

Table 3- Indexes and formulas used in classification

Index	*Formula*	*Equation*	*Reference*
Normalized Difference Vegetation Index	$NDVI = (\rho_{NIR} - \rho_{Red}) / (\rho_{NIR} + \rho_{Red})$	(1)	(Rouse et al. 1974)
Plastic Greenhouse Index	*PGI=0 when NDVI>0.73* $PGI=100 \times \frac{\rho_{Blue} \times (\rho_{NIR} - \rho_{Red})}{1-mean(\rho_{Blue}+\rho_{Green}+\rho_{NIR})}$ *PGI=0 when NDBI>0.005*	(2)	(Yang et al. 2017)
Retrogressive Plastic Greenhouse Index	$RPGI= 100 \times \frac{\rho_{Blue}}{1-mean(\rho_{Blue}+\rho_{Green}+\rho_{NIR})}$	(3)	(Yang et al. 2017)
Plastic Mulched Landcover Index	$PMLI = (\rho_{SWIR} - \rho_{Red}) / (\rho_{SWIR} + \rho_{Red})$	(4)	(Lu et al. 2014)
Greenhouse Vegetable Land Extraction Index	$Vi= \frac{\rho_{SWIR_1}-\rho_{NIR}}{\rho_{SWIR_1}+\rho_{NIR}} \times \frac{\rho_{NIR}-\rho_{red}}{\rho_{NIR}+\rho_{red}}$	(5)	(Zhao GengXing et al. 2004)
In Sentinel-2 MSI satellite images; Blue (B2), Green (B3), Red (B4), NIR (B8), SWIR1 (B11).			

2.3. Random forest algorithm

RF algorithm, developed by (Breiman 2001), is a non-parametric ML method that constructs an ensemble of decision trees. It is widely applied in generating LULC maps from satellite imagery (Kalacska et al. 2020; Li et al. 2016; Millard & Richardson, 2015). The RF algorithm predicts the class of each pixel by leveraging 164abelled training data. During the classification process, it employs the bootstrap aggregation (bagging) technique to generate multiple subsets of the training data, from which individual decision trees are constructed (Belgiu & Drăgu 2016; Lawrence et al. 2006). Final class predictions are determined by majority voting across all trees, thereby enhancing classification accuracy. However, achieving high accuracy is contingent upon the use of a sufficiently large number of trees and high-quality training samples (Pal 2005; Xie et al. 2019). Within the GEE platform, the RF algorithm is readily available in the built-in code library. The classification is performed by specifying key parameters, including the number of trees in the forest (ntree), the maximum number of features considered at each node (mtry), and the maximum depth of each tree (max_depth). In accordance with recommendations from previous studies (Belgiu & Drăgu 2016), ntree was set to 500 to ensure robust model performance. Furthermore, mtry and max_depth were empirically defined as 7 and 16, respectively, to optimize the trade-off between model complexity and generalization capacity.

2.4. Support vector machines algorithm

SVM is supervised classification algorithms based on statistical learning theory and the principle of structural risk minimization (Belgiu & Drăgu 2016; Huang et al. 2002; Pan et al. 2024; M. Zhao et al. 2024). Initially developed for binary classification problems, SVM has since been extended to handle multiclass and non-linear datasets. The algorithm performs classification by identifying the optimal hyperplane that separates the classes (Srivastava et al. 2012; Vapnik 2013). During this process, support vectors and class margins are defined, and a suitable kernel function—such as Linear, Polynomial, Radial Basis Function (RBF), or Sigmoid—is selected to enhance classification performance (Hasituya & Chen 2017; Hasituya et al. 2016). Widely used in RS applications, SVM was implemented in this study using the RBF (SVM-R) kernel, considering the structure and size of the dataset. Furthermore, the gamma (γ) parameter was set to 0.5, and the maximum number of iterations was defined as 10.

2.5. Classification and regression trees algorithm

The CART algorithm is a non-parametric pattern recognition method based on decision trees (Bittencourt & Clarke 2003). Its objective is to partition the dataset into homogeneous subgroups, thereby creating a branching tree structure. At each node, the dataset is split in a way that minimizes variance and maximizes class separability. This structure allows for both classification (categorical variables) and regression (continuous variables) analyses. Predictions within the tree are determined based on the weighted averages at the nodes (Piramuthu 2008). Due to its simple structure, CART is particularly advantageous for small datasets. In this study, it has been implemented in the GEE platform using the "classifier.smileCart" function with a max_depth parameter set to 15.

2.6. Classification accuracy assessment

Accuracy assessment is one of the final and most critical stages in image classification. In the accuracy assessment phase, the agreement between reference maps and the produced LULC map is quantitatively tested (Amini et al. 2022). In this study, classification performance was determined based on OA and *K* values. Additionally, Rc, Pr, F1-S, Spc, and Ac metrics were calculated for each dataset and class produced using ML to determine class accuracies. OA is obtained by dividing the sum of correctly classified pixels for each class by the total number of reference pixels (Equation 6) (Aronoff 1982; G. M. Foody 2020;

Liu et al. 2007; Myint et al. 2011). Here, the incorrectly classified pixels for each class represent the Omission Error (OE). Cohen's *K* statistic (Equation 7), developed by (Cohen 1960), defines overall classification accuracy by considering all elements within the confusion matrix. In this matrix, columns represent reference data, while rows represent classified data. *K* accounts for random agreement between the ground truth and the prediction, and therefore, it is expressed as a simple accuracy value. When tested statistically, the *K* coefficient ranges between 0 and 1. In the context of accuracy assessment, the commonly used evaluation metrics in the literature—Rc (Equation 8), Pr (Equation 9), F1-S (Equation 10), Spc (Equation 11), and Ac (Equation 12)—were calculated separately for each class (Elmahdy et al. 2020). Rc measures the classifier's ability to identify all possible pixels within a class, while Pr refers to the proportion of pixels belonging to the target class that are correctly identified by the classifier. The F1-S, utilized to evaluate classification performance, represents the harmonic mean of Pr and Rc (Ha et al. 2020). Spc represents the proportion of negative pixel classes that are correctly identified, reflecting the model's ability to minimize false positive predictions. It is particularly valuable for evaluating the model's reliability in distinguishing between classes with high spectral similarity (Loukika et al. 2021). Ac is defined as the ratio of correctly classified instances to the total number of instances (Ha et al. 2020).

$$OA=\frac{S_t}{S_n} \text{ x } 100 \quad (6)$$

$$K = nS_t - \sum_{i=1}^{r} \frac{S_{ij}}{n^2} - \sum_{i=1}^{r} S_{ij} \quad (7)$$

Where: S_t denotes the number of correctly classified pixels for any given class. *N*, represents the total number of pixels in the error matrix. *R* signifies the number of rows. S_{ij}, indicates the sum for the i-th row (ground truth) and the j-th column (predicted class label).

$$Recall=\frac{TP}{TP+FN} \quad (8)$$

$$Precision=\frac{TP}{TP+FP} \quad (9)$$

$$F1\text{-}Score=\frac{2\ x\ Precision\ x\ Recall}{Precision+\ Recall} \quad (10)$$

$$Specificity=\frac{TN}{TN+FP} \quad (11)$$

$$Accuracy=\frac{TP+TN}{TP+TN+FP+FN} \quad (12)$$

Where; false negatives (FN), false positives (FP), true positives (TP), and true negatives (TN) refer to the counts of observed instances.

2.7. McNemar test

Initially, OA values were considered to evaluate the performance of indices and ML algorithms used in classification. The statistical significance of the differences in accuracies obtained from the classification was analysed using the McNemar test (Çölkesen et al. 2014). The McNemar test is a non-parametric test based on the chi-square (χ^2) distribution and is calculated using Equation 13. It is also represented by a 2x2 contingency table for pairwise comparisons (M. G. Foody 2004; Gowri & Manjula 2024). If the calculated χ^2 statistic is greater than or equal to the threshold value (χ^2=3.84) at the 95% confidence level (*p*=0.05), there is a statistically significant difference between the compared classification accuracies. In other words, the compared classification accuracies are different from each other. If the calculated χ^2 value is less than the threshold value, there is no statistically significant difference.

$$\chi^2 = \frac{(n_{ij}-n_{ji})^2}{n_{ij}+n_{ji}} \quad (13)$$

In this equation, n_{ij} represents the number of pixels that are incorrectly classified by the *i-th* classifier but correctly classified by the *j-th* classifier, while n_{ji} denotes the number of pixels that are incorrectly classified by the *j-th* classifier but correctly classified by the *i-th* classifier (M. G. Foody 2004).

3. Results

According to the datasets created in this study, a total of 21 LULC maps were produced (Figure 3). The highest accuracy in the classification maps was achieved by classifying the DS3 dataset using the RF ML algorithm, with OA and K statistics of 88.10%

and 0.804, respectively (Table 4). Classifications using traditional bands for RF, CART, and SVM yielded OA values of 73.85%, 80.68% and 84.31% and K values of 0.612, 0.715 and 0.741 respectively. This indicates that the auxiliary datasets positively contributed to classification accuracy, supporting the main hypothesis of the study. The lowest classification accuracy was obtained by classifying the DS2 dataset using the RF algorithm, with OA and K values of 73.10% and 0.608, respectively.

Table 4- Classification performances

		OA	*Kappa (K)*
RF	DS1	73.85%	0.612
SVM		**84.31%**	**0.741**
CART		80.68%	0.715
RF	DS2	73.10%	0.608
SVM		**84.34%**	**0.756**
CART		81.77%	0.734
RF	DS3	**88.10%**	**0.804**
SVM		82.05%	0.736
CART		80.63%	0.712
RF	DS4	76.95%	0.669
SVM		79.83%	0.703
CART		84.09%	0.767
RF	DS5	75.93%	0.655
SVM		79.55%	0.699
CART		80.11%	0.708
RF	DS6	78.10%	0.682
SVM		83.65%	0.760
CART		83.11%	0.752
RF	DS7	76.44%	0.657
SVM		82.62%	0.744
CART		78.92%	0.689

Within the scope of the study, in which greenhouse indices were incorporated to investigate the performance of ML algorithms, classification performance was evaluated using the Rc, Pr, F1-S, Spc, and Ac metrics. An assessment across all datasets revealed substantial variations in classification accuracy among different ML algorithms. For the urban class, in most datasets, the SVM and CART algorithms stood out with both high Rc and Pr. For instance, in DS5, SVM achieved 73% Rc and 92% Pr, yielding the highest F1-S value (0.81). In certain datasets (DS1, DS2, DS6), RF produced high Pr values but suffered from low Rc, resulting in a failure to detect a considerable proportion of urban areas. In DS4, CART achieved 67% Rc and 100% Pr, producing the most successful outcome with no false predictions. The Water class was generally among the most challenging to detect. In DS1, DS3, and DS4, RF yielded very low Rc values (often around 10%), missing the majority of water bodies. Conversely, SVM, which is well-documented as being highly effective in water body detection (Loukika et al. 2021), produced balanced results in DS2 and DS5. In DS4, CART attained 70% Rc and an F1-S of 0.82, successfully identifying a large proportion of water areas. The Bare Land class was classified with high accuracy in most datasets. In DS3, RF achieved 91% Rc and 96% Pr, correctly identifying nearly all bare land pixels. In DS4, CART recorded 96% Rc. This class typically produced high F1-S scores owing to the combination of high Rc and Pr. The Vegetation class exhibited the most consistent success across all datasets. In DS3, SVM reached 99% Rc and 91% Pr, resulting in an F1-S of 0.95. In most cases, all algorithms provided high accuracy for vegetation classification. The agriculture class demonstrated more variable performance. In some datasets (DS1, DS6), CART produced more balanced and higher F1-S values. RF generally yielded high Rc but lower Pr, increasing the false positive rate. In certain datasets, SVM produced relatively low F1-S values, indicating difficulty in accurately identifying agricultural areas. The Greenhouse class was classified with high accuracy in most datasets. In DS1, DS6, and DS7, both RF and SVM achieved Rc values above 90% and Pr values of 100%, enabling them to detect greenhouse areas at very high rates without any false predictions. In DS4, SVM and CART achieved 80% Rc and 100% Pr, producing near-perfect classification outcomes. The complete set of classification performance metrics is presented in Tables 5–11. Based on the accuracy measures, the Urban and Water classes posed the greatest classification challenges, as reflected by the low Rc values across algorithms. The agriculture class exhibited notable inconsistencies between algorithms, primarily due to spectral overlap leading to confusion between bare land and agricultural areas. While Bare Land and Vegetation were classified with high accuracy by nearly all algorithms, Greenhouse emerged as the most reliably classified class, with consistently high Rc and Pr values (Loukika et al. 2021).

Table 5- Classification performance metrics based on DS1

LULC	*RF*					*SVM*					*CART*				
	DS1					*DS1*					*DS1*				
	Rc(%)	***Pr(%)***	***F1-S***	***Spc***	***Ac***	***Rc(%)***	***Pr(%)***	***F1-S***	***Spc***	***Ac***	***Rc(%)***	***Pr(%)***	***F1-S***	***Spc***	***Ac***
Urban	15%	80%	0.25	0.93	0.93	75%	86%	0.80	0.99	0.99	47%	100%	0.64	0.98	0.98
Water	10%	33%	0.15	0.97	0.97	50%	100%	0.67	0.99	0.99	50%	100%	0.67	0.99	0.99
Bare land	81%	59%	0.68	0.92	0.80	80%	89%	0.84	0.86	0.87	89%	69%	0.78	0.96	0.87
Vegetation	98%	89%	0.93	0.98	0.94	93%	90%	0.91	0.94	0.92	99%	89%	0.94	0.99	0.94
Agriculture	43%	57%	0.49	0.90	0.86	54%	21%	0.30	0.99	0.93	47%	71%	0.57	0.87	0.84
Greenhouse	50%	100%	0.67	0.98	0.98	70%	88%	0.78	0.99	0.99	70%	100%	0.82	0.99	0.99
(OA)=	73.85%					84.31%					80.68%				
(***K***)	0.612					0.741					0.715				

Table 6- Classification performance metrics based on DS2

LULC	*RF*					*SVM*					*CART*				
	DS2					*DS2*					*DS2*				
	Rc(%)	***Pr(%)***	***F1-S***	***Spc***	***Ac***	***Rc(%)***	***Pr(%)***	***F1-S***	***Spc***	***Ac***	***Rc(%)***	***Pr(%)***	***F1-S***	***Spc***	***Ac***
Urban	36%	100%	0.53	0.95	0.95	60%	86%	0.71	0.99	0.98	47%	78%	0.58	0.98	0.97
Water	30%	100%	0.46	0.98	0.98	86%	100%	0.92	1.00	1.00	50%	100%	0.67	0.99	0.99
Bare land	80%	61%	0.69	0.92	0.80	84%	82%	0.83	0.91	0.88	90%	66%	0.76	0.96	0.86
Vegetation	97%	85%	0.91	0.97	0.92	98%	92%	0.95	0.98	0.95	97%	95%	0.96	0.98	0.97
Agriculture	32%	52%	0.40	0.86	0.82	33%	43%	0.38	0.93	0.89	54%	79%	0.64	0.88	0.87
Greenhouse	70%	78%	0.74	0.99	0.99	80%	89%	0.84	0.99	0.99	70%	78%	0.74	0.99	0.99
(OA)=	73.10%					84.34%					81.77%				
(***K***)	0.608					0.756					0.734				

Table 7- Classification performance metrics based on DS3

LULC	*RF*					*SVM*					*CART*				
	DS3					*DS3*					*DS3*				
	Rc(%)	***Pr (%)***	***F1-S***	***Spc***	***Ac***	***Rc(%)***	***Pr(%)***	***F1-S***	***Spc***	***Ac***	***Rc(%)***	***Pr(%)***	***F1-S***	***Spc***	***Ac***
Urban	60%	86%	0.71	0.99	0.99	27%	100%	0.42	0.97	0.97	40%	86%	0.55	0.97	0.97
Water	10%	100%	0.18	0.97	0.97	30%	60%	0.40	0.98	0.97	50%	100%	0.67	0.99	0.99
Bare land	91%	96%	0.93	0.89	0.93	96%	64%	0.77	0.99	0.88	92%	66%	0.77	0.97	0.86
Vegetation	99%	86%	0.92	1.00	0.95	99%	91%	0.95	0.99	0.95	98%	91%	0.94	0.98	0.95
Agriculture	63%	48%	0.55	0.97	0.93	53%	92%	0.67	0.87	0.87	39%	75%	0.51	0.86	0.85
Greenhouse	90%	100%	0.95	1.00	1.00	90%	90%	0.90	1.00	0.99	90%	100%	0.95	1.00	1.00
(OA)=	**88.10%**					82.05%					80.63%				
(***K***)	**0.804**					0.736					0.712				

Table 8- Classification performance metrics based on DS4

LULC	*RF*					*SVM*					*CART*				
	DS4					*DS4*					*DS4*				
	Rc(%)	***Pr(%)***	***F1-S***	***Spc***	***Ac***	***Rc(%)***	***Pr(%)***	***F1-S***	***Spc***	***Ac***	***Rc(%)***	***Pr(%)***	***F1-S***	***Spc***	***Ac***
Urban	43%	91%	0.59	0.96	0.96	33%	71%	0.45	0.97	0.97	67%	100%	0.80	0.99	0.99
Water	10%	100%	0.18	0.97	0.97	50%	100%	0.67	0.99	0.99	70%	100%	0.82	0.99	0.99
Bare land	89%	63%	0.73	0.96	0.84	91%	65%	0.75	0.97	0.86	96%	71%	0.82	0.99	0.89
Vegetation	97%	88%	0.92	0.98	0.93	99%	89%	0.94	0.99	0.94	99%	90%	0.94	0.99	0.95
Agriculture	48%	76%	0.59	0.87	0.85	44%	80%	0.57	0.86	0.85	48%	88%	0.62	0.87	0.87
Greenhouse	60%	75%	0.67	0.99	0.98	80%	100%	0.89	0.99	0.99	80%	100%	0.89	0.99	0.99
(OA)=	76.95%					79.83%					84.09%				
(***K***)	0.669					0.703					0.767				

Table 9- Classification performance metrics based on DS5

LULC	*RF*					*SVM*					*CART*				
	DS5					*DS5*					*DS5*				
	Rc (%)	***Pr (%)***	***F1-S***	***Spc***	***Ac***	***Rc (%)***	***Pr (%)***	***F1-S***	***Spc***	***Ac***	***Rc (%)***	***Pr (%)***	***F1-S***	***Spc***	***Ac***
Urban	39%	90%	0.55	0.96	0.96	73%	92%	0.81	0.99	0.99	40%	86%	0.55	0.97	0.97
Water	30%	100%	0.46	0.98	0.98	40%	100%	0.57	0.98	0.98	60%	100%	0.75	0.99	0.99
Bare land	88%	60%	0.71	0.95	0.81	91%	67%	0.77	0.97	0.87	90%	65%	0.75	0.96	0.86
Vegetation	96%	91%	0.93	0.97	0.95	99%	88%	0.93	0.99	0.93	99%	90%	0.95	0.99	0.95
Agriculture	42%	69%	0.52	0.86	0.84	35%	71%	0.47	0.84	0.83	40%	78%	0.53	0.85	0.84
Greenhouse	70%	88%	0.78	0.99	0.99	80%	100%	0.89	0.99	0.99	90%	82%	0.86	1.00	0.99
(OA)=	75.93%					79.55%					80.11%				
(***K***)	0.655					0.699					0.708				

Table 10- Classification performance metrics based on DS6

LULC	*RF*					*SVM*					*CART*				
	DS6					*DS6*					*DS6*				
	Rc (%)	***Pr (%)***	***F1-S***	***Spc***	***Ac***	***Rc (%)***	***Pr (%)***	***F1-S***	***Spc***	***Ac***	***Rc (%)***	***Pr (%)***	***F1-S***	***Spc***	***Ac***
Urban	39%	100%	0.56	0.96	0.96	63%	100%	0.77	0.98	0.98	63%	100%	0.77	0.98	0.98
Water	20%	100%	0.33	0.98	0.98	60%	86%	0.71	0.99	0.99	50%	100%	0.67	0.99	0.99
Bare land	90%	65%	0.75	0.96	0.85	92%	72%	0.81	0.97	0.89	90%	69%	0.79	0.96	0.88
Vegetation	98%	86%	0.92	0.98	0.93	98%	91%	0.94	0.98	0.95	98%	92%	0.95	0.98	0.95
Agriculture	43%	76%	0.55	0.87	0.85	51%	80%	0.62	0.88	0.87	54%	79%	0.64	0.88	0.87
Greenhouse	90%	100%	0.95	1.00	1.00	90%	100%	0.95	1.00	1.00	80%	100%	0.89	0.99	0.99
(OA)=	78.10%					84.65%					83.11%				
(***K***)	0.682					0.760					0.752				

Table 11- Classification performance metrics based on DS7

LULC	*RF*					*SVM*					*CART*				
	DS7					*DS7*					*DS7*				
	Rc (%)	***Pr (%)***	***F1-S***	***Spc***	***Ac***	***Rc (%)***	***Pr (%)***	***F1-S***	***Spc***	***Ac***	***Rc (%)***	***Pr (%)***	***F1-S***	***Spc***	***Ac***
Urban	19%	63%	0.29	0.94	0.93	40%	86%	0.55	0.97	0.97	47%	70%	0.56	0.98	0.97
Water	30%	75%	0.43	0.98	0.98	60%	100%	0.75	0.99	0.99	50%	100%	0.67	0.99	0.99
Bare land	92%	64%	0.76	0.96	0.84	92%	66%	0.77	0.97	0.86	87%	64%	0.74	0.95	0.85
Vegetation	98%	89%	0.93	0.98	0.94	100%	95%	0.98	1.00	0.98	99%	92%	0.95	0.99	0.95
Agriculture	40%	67%	0.50	0.87	0.85	47%	79%	0.59	0.87	0.86	38%	68%	0.49	0.85	0.83
Greenhouse	60%	100%	0.75	0.99	0.99	80%	89%	0.84	0.99	0.99	70%	78%	0.74	0.99	0.99
(OA)=	76.44%					82.62%					78.92%				
(***K***)	0.657					0.744					0.689				

The RF algorithm can be easily applied to high-dimensional datasets and requires less training data compared to other algorithms (Gislason et al. 2006; Goldblatt et al. 2016, 2018; Guan et al. 2013). For this reason, it has produced superior results compared to other classification algorithms. This is particularly significant for classification processes involving the detection of greenhouse-covered land surfaces, where the inclusion of the PGI index serves as a reference. Here, the Rc, Pr, F1-S, Spc, and Ac values for greenhouse areas are 90%, 100%, 0.95, 1.00, and 1.00, respectively. These findings highlight the ability of the RF algorithm, together with PGI, to distinguish land cover classes, including greenhouses. In this study, a classification map was produced using the dataset with the highest model accuracy (Figure 4). The resulting map was converted from raster to vector data format using ArcGIS Pro 3.2 software, and the areas of each class were calculated. Based on the calculated areas, the land cover classes and their proportions within the total area were determined as follows: urban 1% (138 km²), water 1% (147 km²), bare land 58% (111,742 km²), vegetation 32% (6,581 km²), agriculture 7% (1,336 km²), and greenhouse 2% (408 km²) (Figure 5).

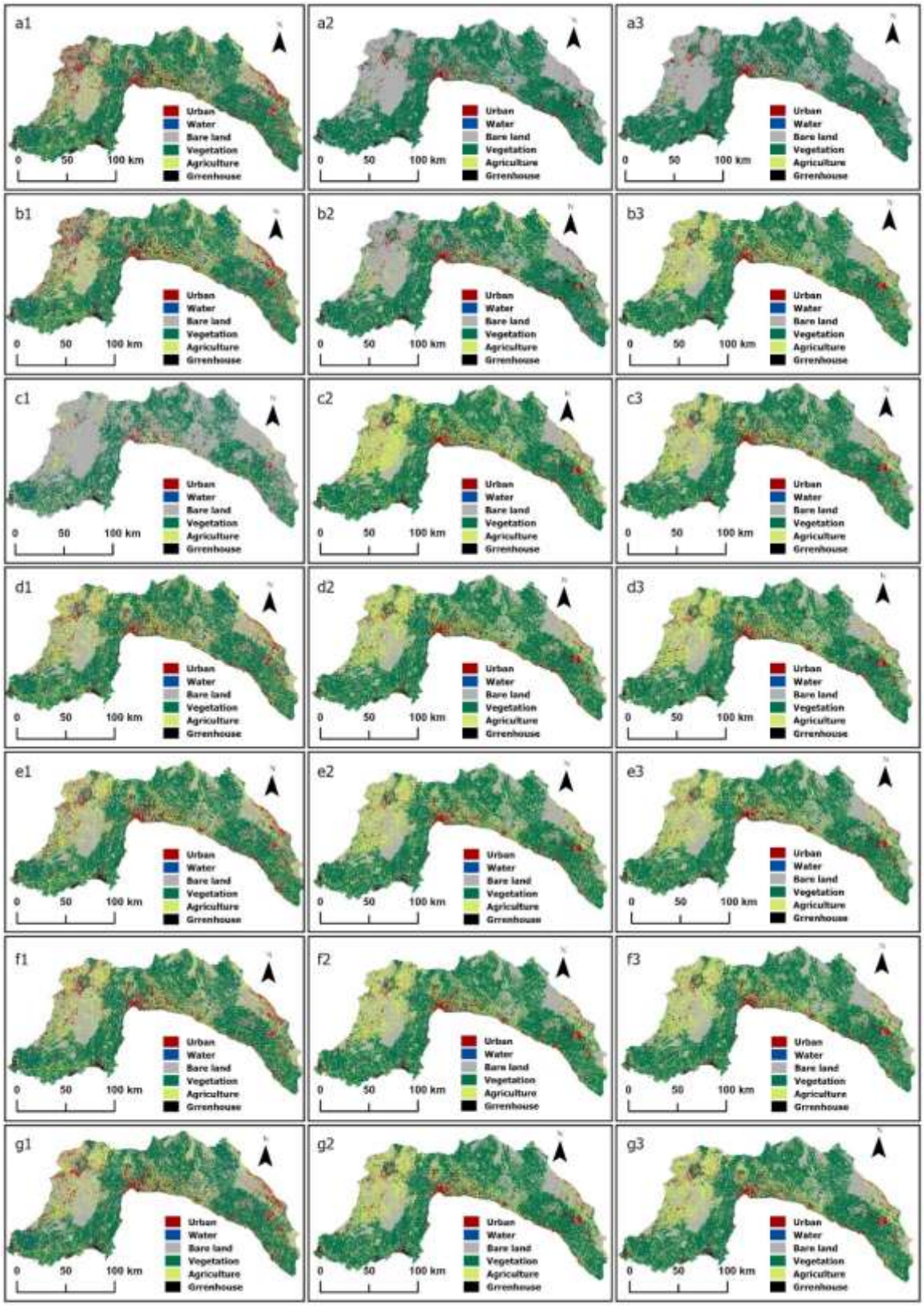

Figure 3- a, b, c, d, e, f and g present the classification maps generated using datasets DS1, DS2, DS3, DS4, DS5, DS6, and DS7, respectively, with the RF (1), SVM (2), and CART (3) machine learning algorithms

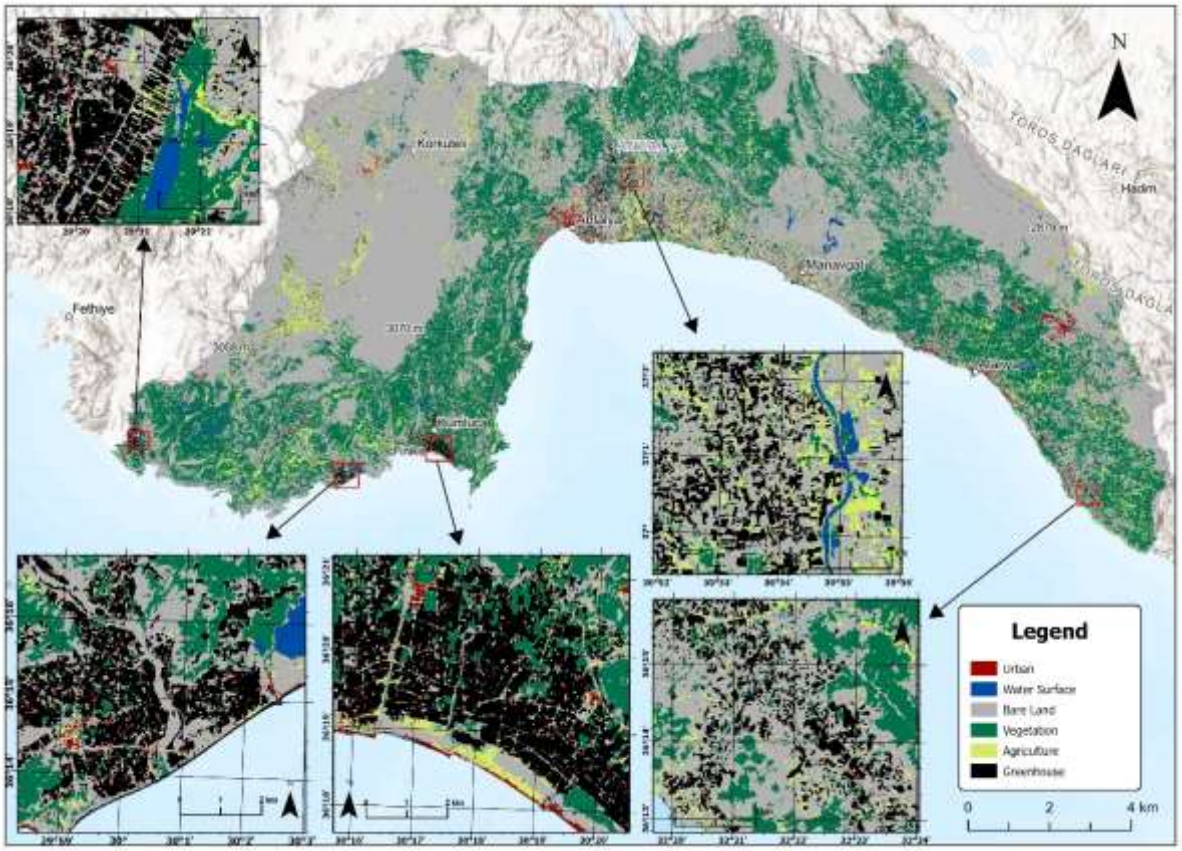

Figure 4- Greenhouse map of the study area

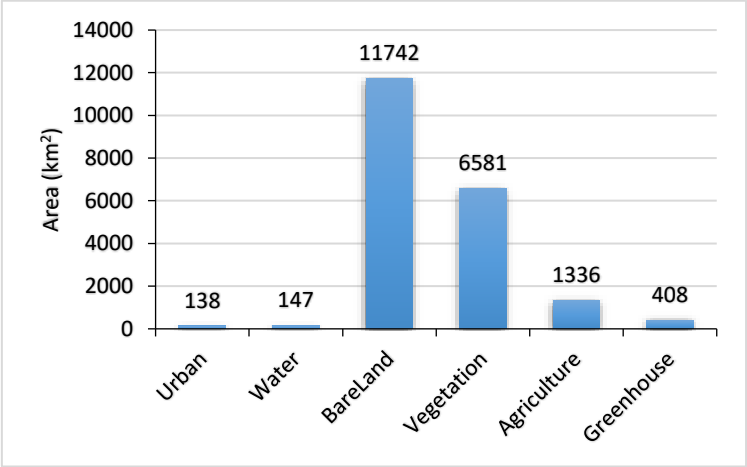

Figure 5- Area of LULC classes using PGI and RF

The results of the McNemar tests, conducted separately for each index and classifier, are presented in Table 12 to determine whether there are statistically significant differences between the classification accuracies of the indices and ML algorithms used for greenhouse detection in the study. A calculated statistic value greater than the χ^2 table value at the 95% confidence interval indicates statistically significant results (M. G. Foody 2004).

Table 12- McNemar test result

Data Set	RF-DS1	SVM-DS1	CART-DS1	RF-DS2	SVM-DS2	CART-DS2	RF-DS3	SVM-DS3	CART-DS3	RF-DS4	SVM-DS4	CART-DS4	RF-DS5	SVM-DS5	CART-DS5	RF-DS6	SVM-DS6	CART-DS6	RF-DS7	SVM-DS7	CART-DS7
RF-DS1		0.00	**4.92**	0.00	**10.61**	**6.51**	**21.06**	**6.51**	**4.07**	0.90	3.36	**10.23**	0.92	**3.31**	**5.28**	2.83	**9.08**	**7.13**	0.95	**7.47**	2.68
SVM-DS1	1.00		**3.87**	0.03	**9.07**	**5.19**	**19.06**	**5.28**	3.11	0.48	2.49	**8.74**	0.45	2.45	**4.08**	1.94	**7.69**	**5.78**	0.51	**6.13**	1.91
CART-DS1	0.03	0.05		**5.70**	0.35	0.10	**6.65**	0.16	0.00	1.03	0.03	1.59	1.68	0.09	0.01	0.45	0.81	0.23	1.62	0.34	0.24
RF-DS2	1.00	0.85	0.02		**11.68**	**7.17**	**25.81**	**8.64**	**6.27**	1.79	**4.73**	**13.45**	1.12	**4.61**	**5.32**	2.84	**11.74**	**9.57**	1.52	**10.37**	**3.89**
SVM-DS2	0.00	0.00	0.55	0.00		0.04	3.68	0.00	0.25	2.26	0.59	0.24	3.68	0.76	0.44	1.51	0.08	0.00	2.82	0.01	0.84
CART-DS2	0.01	0.02	0.75	0.01	0.85		**4.89**	0.01	0.04	1.80	0.22	0.69	2.68	0.36	0.15	0.88	0.36	0.08	2.23	0.17	0.44
RF-DS3	0.00	0.00	0.01	0.00	0.05	0.03		**4.30**	**6.38**	**13.69**	**8.25**	2.22	**15.28**	**8.95**	**8.28**	**10.89**	2.34	3.56	**13.83**	3.44	**8.41**
SVM-DS3	0.01	0.02	0.69	0.00	1.00	0.92	0.04		0.16	2.49	0.45	0.38	3.48	0.59	0.34	1.27	0.16	0.01	2.72	0.04	0.68
CART-DS3	0.04	0.08	1.00	0.01	0.62	0.85	0.01	0.68		1.06	0.04	1.21	1.94	0.09	0.01	0.44	0.83	0.32	1.43	0.45	0.14
RF-DS4	0.34	0.49	0.31	0.18	0.13	0.18	0.00	0.11	0.30		0.56	4.41	0.07	0.40	0.68	0.07	**4.32**	2.82	0.01	3.22	0.27
SVM-DS4	0.07	0.11	0.85	0.03	0.44	0.64	0.00	0.50	0.84	0.46		1.87	1.40	0.00	0.00	0.14	1.25	0.75	0.87	0.88	0.01
CART-DS4	0.00	0.00	0.21	0.00	0.62	0.41	0.14	0.54	0.27	0.04	0.17		**6.28**	2.21	1.63	3.22	0.01	0.15	**5.58**	0.09	2.23
RF-DS5	0.34	0.50	0.20	0.29	0.06	0.10	0.00	0.06	0.16	0.79	0.24	0.01		0.89	1.56	0.42	**5.04**	**4.14**	0.01	**4.72**	0.74
SVM-DS5	0.07	0.12	0.76	0.03	0.38	0.55	0.00	0.44	0.77	0.53	1.00	0.14	0.35		0.01	0.08	1.59	0.88	0.72	1.34	0.00
CART-DS5	0.02	0.04	0.93	0.02	0.51	0.70	0.00	0.56	0.92	0.41	1.00	0.20	0.21	0.93		0.24	1.04	0.58	1.01	0.71	0.03
RF-DS6	0.09	0.16	0.50	0.09	0.22	0.35	0.00	0.26	0.51	0.79	0.71	0.07	0.52	0.78	0.63		2.68	1.70	0.18	1.97	0.03
SVM-DS6	0.00	0.01	0.37	0.00	0.77	0.55	0.13	0.69	0.36	0.04	0.26	0.92	0.02	0.21	0.31	0.10		0.01	**3.93**	0.00	1.54
CART-DS6	0.01	0.02	0.63	0.00	1.00	0.77	0.06	0.92	0.57	0.09	0.39	0.70	0.04	0.35	0.45	0.19	0.92		3.54	0.00	1.04
RF-DS7	0.33	0.47	0.20	0.22	0.09	0.14	0.00	0.10	0.23	0.93	0.35	0.02	0.93	0.40	0.32	0.67	0.05	0.06		**3.94**	0.55
SVM-DS7	0.01	0.01	0.56	0.00	0.92	0.68	0.06	0.85	0.50	0.07	0.35	0.76	0.03	0.25	0.40	0.16	1.00	1.00	0.05		1.55
CART-DS7	0.10	0.17	0.62	0.05	0.36	0.51	0.00	0.41	0.71	0.60	0.93	0.14	0.39	1.00	0.87	0.86	0.22	0.31	0.46	0.21	

The values below the diagonal in the comparison matrix represent the p-values, while those above the diagonal represent the χ^2 values.

When the results of the RF algorithm applied to DS3, which achieved the highest OA and $\boldsymbol{K}$ values, were compared to classifications performed with other ML algorithms and datasets; statistically significant differences were found between DS3+SVM, DS3+CART, DS4+RF, DS4+SVM, DS5+RF, DS5+SVM, DS5+CART, DS6+RF, DS7+RF, and DS7+CART. In all comparisons where the χ^2 value exceeded the 3.84 threshold, the use of DS2 and the RF algorithm resulted in a significant improvement in accuracy at the $p < 0.05$ (95% confidence level) when compared to using other datasets and ML algorithms. In this case, no significant difference was observed between the classification using the RF algorithm on the DS3 dataset and the classifications obtained with the DS2+SVM, DS4+CART, DS6+SVM, DS6+CART, and DS7+SVM algorithms.

4. Discussion

In recent years, numerous studies have been conducted using various data sources for the generation of LULC maps and the detection of greenhouse areas. These studies have significantly enhanced classification accuracy, particularly by developing spectral indices aimed at improving the identification of specific land cover classes. In this context, investigating the classification of greenhouse areas at different scales and examining the effectiveness of the indices employed holds substantial promise for guiding future research.

In this study, the combination of the PGI and the RF ML algorithm achieved the highest classification performance, with an OA of 88.10%. This accuracy exceeds the performance obtained using the SVM and CART algorithms. The superior performance of the RF algorithm is consistent with findings from previous studies. For instance, (Cui et al. 2022) reported an OA of 95.85%, (Ou et al. 2020) reported 90%, and (Rodriguez-Galiano et al. 2012) reported 92%. These results demonstrate that the RF algorithm consistently delivers high classification accuracy across various contexts, further validating the outcomes of the present study.

The OA obtained exceeds the commonly accepted threshold of 85% for classification accuracy, as suggested by (Kpienbaareh et al. 2021). The superior performance of the RF algorithm is attributed to its robustness against overfitting and its capability to handle high-dimensional datasets. Similarly, (Koc-San 2013) employed RF for high-dimensional data involving both plastic and glass greenhouses and achieved an accuracy of 91%, corroborating the findings of this study. The RF algorithm, which utilizes an ensemble learning approach, demonstrates exceptional performance in accurately classifying land cover and managing large-scale geospatial datasets (Pal & Foody 2012). Furthermore, factors such as bootstrap sampling, an increased number of decision trees, and random feature selection enhance the model's performance (Talukdar et al. 2020). In contrast, the CART algorithm exhibited lower classification accuracy in the current study when compared to RF and SVM. This result may be explained by CART's susceptibility to overfitting and its sensitivity to small variations in the training dataset (Prasad et al. 2006). The

relatively higher accuracy achieved by RF and SVM can be attributed to their greater tolerance to both random and systematic noise within the training data (Camargo et al. 2019; Pelletier et al. 2017). The SVM algorithm, while particularly effective in high-dimensional datasets and when class boundaries are well-defined, is associated with certain limitations such as long training times for large datasets, and challenges in model tuning and interpretation (Huang et al. 2002).

The study incorporates indices such as PGI and RPGI, which were specifically developed for the detection of plastic greenhouse structures and have been utilized in a limited number of studies in the literature (Li et al. 2023). The integration of the PGI—an index specifically developed for greenhouse detection—into the classification process significantly improved the distinction of greenhouses from other land cover classes. This finding is consistent with the literature emphasizing the contribution of customized spectral indices to classification accuracy (Zarco-Tejada et al. 2012). Similarly, (Veettil & Xuan 2022) reported a 90% OA when incorporating the PGI into the classification, enhancing overall performance. In line with these findings, the current study also revealed that the threshold values applied to the PGI effectively differentiated greenhouse structures from both agricultural plastic-covered facilities and urban buildings. The high performance achieved using PGI and the RF algorithm is directly linked to the integration of ancillary data in the classification process. This integration notably enhanced the separability of spectrally similar classes such as bare soil and croplands. This observation is in agreement with the findings of (Acharki 2022). Additionally, the combination of the NDVI and the SVM algorithm demonstrated high accuracy in the identification of water bodies, yielding an F1-S of 0.92. This result aligns with previous studies highlighting the SVM algorithm's effectiveness in delineating water surfaces from other classes due to its margin-maximizing properties (García Nieto et al. 2014; Loukika et al. 2021). On the other hand, it is well-documented that the SVM algorithm tends to perform less accurately in urban areas (Ouma et al. 2022). However, in the current study, the use of auxiliary datasets positively contributed to SVM's performance, demonstrating its efficiency in handling high-dimensional data with well-defined interclass differences. The incorporation of all spectral indices with the SVM algorithm also improved the accuracy of vegetation classification, with the highest F1-S for vegetation (0.98) obtained using this combination. This success is primarily attributed to the inclusion of Red-Edge and NIR bands in the dataset, which are known to reflect the physiological condition of vegetation (Gislason et al. 2006). Nevertheless, all ML algorithms used in this study encountered challenges in distinguishing between bare soil and cropland. This situation has led to pronounced disparities in F1-S values across classes. Specifically, the observed outcome can be attributed to spectral overlap, wherein the classes in question exhibit similar reflectance characteristics within the visible bands. As emphasized by (Chlouveraki et al. 2025) and (Delaney et al. 2025), hyperspectral imaging techniques face challenges in discriminating textural differences in areas characterized by sparse vegetation cover. Future studies are expected to achieve more accurate differentiation between these classes through the integration of multi-temporal datasets such as NDVI time series and the application of advanced machine learning algorithms (Hasituya & Chen, 2017) As emphasized in prior studies, classification performance varies significantly across different ML algorithms—even when using the same dataset and temporal span (Abdi 2020; Tariq et al. 2023). The findings of the current study also reflect such variations, highlighting the strengths and limitations of each algorithm across different LULC classes.

5. Conclusions

Greenhouses, widely utilized in agricultural production, significantly enhance crop yield. However, the increasing prevalence of greenhouses has led to a number of environmental concerns. Consequently, the mapping of greenhouse areas using RS techniques has attracted the attention of various disciplines. In this context, GEE offers a substantial advantage by minimizing the costs associated with the processing and analysis of satellite imagery. Despite this, limited research has been conducted on the detection of greenhouse areas using the GEE platform. The present study provides a comparative evaluation of different greenhouse-specific spectral indices and ML algorithms. The findings indicate that the combination of the PGI and the RF algorithm yielded the highest classification accuracy compared to other algorithms and indices. This combination proved particularly effective in distinguishing greenhouse areas from other land cover types and aligns well with the results of similar studies in the literature. Additionally, the size of the dataset, the quality of training samples, and the spatial extent of the study area were identified as influential factors in classifier selection. The superior performance of the RF algorithm over SVM and CART was attributed to the use of a larger training dataset and the integration of ancillary data sources into the classification process.

While the present study successfully evaluates the classification accuracy of various ML algorithms and spectral indices for greenhouse detection, it also presents several limitations. First, the analysis was conducted over a single temporal period, which may not fully capture the phenological variability typical of agricultural areas. In particular, confusion between spectrally similar classes such as croplands and bare soil could be mitigated through the use of NDVI time series. Furthermore, Sentinel-2 imagery has demonstrated limitations in accurately delineating small and complex greenhouse boundaries. In high-altitude regions, persistent snow cover has caused spectral confusion between greenhouses and snow, negatively impacting classification accuracy. Secondly, the applicability of the PGI and RF combination has not yet been tested under varying greenhouse types, atmospheric conditions, and environmental contexts across different regions. Therefore, further validation across diverse geographic areas and temporal scales is necessary. Moreover, the incorporation of very high-resolution satellite imagery (e.g., WorldView-3, GeoEye-1, Pleiades-1A and 1B, QuickBird) and additional spectral indices may further enhance classification performance.

Author Declarations

Authors' contributions: Concept: GR., Design: SFB, Data collection: GR, Analysis: YOS, Writing: GR & AAM.

Conflict of interest/Competing interests: The author(s) declare no conflict of interest.

Ethics approval/declarations: No need.

Funding: This research received no external funding.

Consent to participate: No need.

Consent for publication: No need.

Data availability: Data are available on request due to privacy or other restrictions.

References

Abdi A M (2020). Land cover and land use classification performance of machine learning algorithms in a boreal landscape using Sentinel-2 data. *GIScience and Remote Sensing* 57(1): 1–20. https://doi.org/10.1080/15481603.2019.1650447

Acharki S (2022). PlanetScope contributions compared to Sentinel-2, and Landsat-8 for LULC mapping. *Remote Sensing Applications: Society and Environment* 27, 100774. https://doi.org/10.1016/j.rsase.2022.100774

Aguilar M A, Jiménez-Lao R & Aguilar F J (2021). Evaluation of Object-Based Greenhouse Mapping Using WorldView-3 VNIR and SWIR Data: A Case Study fromAlmería (Spain). *Remote Sensing* 13(11). https://doi.org/10.3390/rs13112133

Aguilar M A, Nemmaoui A, Novelli A, Aguilar F J & Lorca A G (2016). Object-based greenhouse mapping using very high resolution satellite data and Landsat 8 time series. *Remote Sensing* 8(6). https://doi.org/10.3390/rs8060513

Aguilar M A, Vallario A, Aguilar F J, Lorca A G & Parente C (2015). Object-based greenhouse horticultural crop identification from multi-temporal satellite imagery: A case study in Almeria, Spain. *Remote Sensing* 7(6): 7378–7401. https://doi.org/10.3390/rs70607378

Al-Najjar H A H, Kalantar B, Pradhan B, Saeidi V, Halin A A, Ueda N & Mansor S (2019). Land cover classification from fused DSM and UAV images using convolutional neural networks. *Remote Sensing* 11(12): https://doi.org/10.3390/rs11121461

Amini S, Saber M, Rabiei-Dastjerdi H & Homayouni S (2022). Urban Land Use and Land Cover Change Analysis Using Random Forest Classification of Landsat Time Series. *Remote Sensing*, 14(11). https://doi.org/10.3390/rs14112654

Aronoff S (1982). Classification accuracy: a user approach. *Photogrammetric Engineering and Remote Sensing* 48(8): 1299–1307

Avtar R, Tripathi S, Aggarwal A K & Kumar P (2019). Population-urbanization-energy nexus: A review. In *Resources* 8(3). https://doi.org/10.3390/resources8030136

Ayazli I E (2024). Investigating the interactions between spatiotemporal land use/land cover dynamics and private land ownership. *Land Use Policy* 141, 107165. https://doi.org/10.1016/j.landusepol.2024.107165

Belgiu M & Drăgu L (2016). Random forest in remote sensing: A review of applications and future directions. *ISPRS Journal of Photogrammetry and Remote Sensing* 114: 24–31. https://doi.org/10.1016/J.ISPRSJPRS.2016.01.011

Bittencourt H R & Clarke R T (2003). Use of classification and regression trees (CART) to classify remotely-sensed digital images. *IGARSS 2003. 2003 IEEE International Geoscience and Remote Sensing Symposium* 6: 3751–3753. https://doi.org/10.1109/IGARSS.2003.1295258

Breiman L (2001). Random forests. *Machine Learning* 45: 5–32

Camargo F F, Sano E E, Almeida C M, Mura J C & Almeida T (2019). A comparative assessment of machine-learning techniques for land use and land cover classification of the Brazilian tropical savanna using ALOS-2/PALSAR-2 polarimetric images. *Remote Sensing* 11(13). https://doi.org/10.3390/rs11131600

Castaldi F, Palombo A, Santini F, Pascucci S, Pignatti S & Casa R (2016). Evaluation of the potential of the current and forthcoming multispectral and hyperspectral imagers to estimate soil texture and organic carbon. *Remote Sensing of Environment* 179: 54–65. https://doi.org/10.1016/J.RSE.2016.03.025

Chlouveraki E, Katsenios N, Efthimiadou A, Lazarou E, Kounani K, Papakonstantinou E, Vlachakis D, Kasimati A, Zafeiriou I, Espejo-Garcia B & Fountas S (2025). Estimation of soil properties using Hyperspectral imaging and Machine learning. *Smart Agricultural Technology* 10, 100790. https://doi.org/10.1016/J.ATECH.2025.100790

Cohen J (1960). A coefficient of agreement for nominal scales. *Educational and Psychological Measurement* 20(1): 37–46

Çölkesen I, Yomralioglu T & Kavzoglu T (2014). Classification of Multispectral High-Resolution Satellite Imagery Using Rotation Forest Algorithm. *V. Remote Sensing and Geographic Information Systems Symposium*.

CuiB, Huang W J, Ye H C, Chen Q X, Li Z C & Jiang H Y (2022). Optimal Spatial Resolution of Remote-Sensing Imagery for Monitoring Cantaloupe Greenhouses. *IOP Conference Series: Earth and Environmental Science* 1004(1). https://doi.org/10.1088/1755-1315/1004/1/012020

Delaney B, Tansey K & Whelan M (2025). Satellite Remote Sensing Techniques and Limitations for Identifying Bare Soil. In *Remote Sensing* 17 (4). https://doi.org/10.3390/rs17040630

Demattê J A M, Fongaro C T, Rizzo R & Safanelli J L (2018). Geospatial Soil Sensing System (GEOS3): A powerful data mining procedure to retrieve soil spectral reflectance from satellite images. *Remote Sensing of Environment* 212: 161–175. https://doi.org/10.1016/J.RSE.2018.04.047

Djamai N & Fernandes R (2018). Comparison of SNAP-derived Sentinel-2A L2A product to ESA product over Europe. In *Remote Sensing* 10 (6). https://doi.org/10.3390/rs10060926

Dou P, Shen H, Li Z, & Guan X (2021). Time series remote sensing image classification framework using combination of deep learning and multiple classifiers system. *International Journal of Applied Earth Observation and Geoinformation* 103, 102477. https://doi.org/10.1016/J.JAG.2021.102477

Drusch M, Del Bello U, Carlier S, Colin O, Fernandez V, Gascon F, Hoersch B, Isola C, Laberinti P, Martimort P, Meygret A, Spoto F, Sy O, Marchese F & Bargellini P (2012). Sentinel-2: ESA's Optical High-Resolution Mission for GMES Operational Services. *Remote Sensing of Environment* 120: 25–36. https://doi.org/10.1016/J.RSE.2011.11.026

Elmahdy S, Mohamed M & Ali T (2020). Land use/land cover changes impact on groundwater level and quality in the northern part of the United Arab Emirates. *Remote Sensing* 12(11). https://doi.org/10.3390/rs12111715

Foody G M (2020). Explaining the unsuitability of the kappa coefficient in the assessment and comparison of the accuracy of thematic maps obtained by image classification. *Remote Sensing of Environment* 239, 111630. https://doi.org/10.1016/J.RSE.2019.111630

Foody M G (2004). Thematic Map Comparison: Evaluating the Statistical Significance of Differences in Classification Accuracy. *Photogrammetric Engineering and Remote Sensing* 70(5): 627–633

Gao C, Wu Q, Dyck M, Fang L & He H (2022). Greenhouses Detection in Guanzhong Plain, Shaanxi, China: Evaluation of Four Classification Methods in Google Earth Engine. *Canadian Journal of Remote Sensing* 48(6): 747–763. https://doi.org/10.1080/07038992.2022.2117687

García Nieto P J, García-Gonzalo E, Alonso Fernández J R & Díaz Muñiz C (2014). Hybrid PSO–SVM-based method for long-term forecasting of turbidity in the Nalón river basin: A case study in Northern Spain. *Ecological Engineering*, 73: 192–200. https://doi.org/10.1016/J.ECOLENG.2014.09.042

Gislason P O, Benediktsson J A & Sveinsson J R (2006). Random Forests for land cover classification. *Pattern Recognition Letters*, 27(4): 294–300. https://doi.org/10.1016/J.PATREC.2005.08.011

Goldblatt R, Stuhlmacher M F, Tellman B, Clinton N, Hanson G, Georgescu M, Wang C, Serrano-Candela F, Khandelwal A K, Cheng W H & Balling R C (2018). Using Landsat and nighttime lights for supervised pixel-based image classification of urban land cover. *Remote Sensing of Environment* 205: 253–275. https://doi.org/10.1016/J.RSE.2017.11.026

Goldblatt R, You W, Hanson G & Khandelwal A K (2016a). Detecting the boundaries of urban areas in India: A dataset for pixel-based image classification in google earth engine. *Remote Sensing* 8(8). https://doi.org/10.3390/rs8080634

González-Yebra Ó, Aguilar M A, Nemmaoui A & Aguilar F J (2018). Methodological Proposal to Assess Plastic Greenhouses Land Cover Change from the Combination of Archival Aerial Orthoimages and Landsat Data. *Biosystems Engineering* 175: 36–51. https://doi.org/10.1016/j.biosystemseng.2018.08.009

Gorelick N, Hancher M, Dixon M, Ilyushchenko S, Thau D & Moore R (2017). Google Earth Engine: Planetary-scale geospatial analysis for everyone. *Remote Sensing of Environment* 202: 18–27. https://doi.org/10.1016/J.RSE.2017.06.031

Gowri L & Manjula K R (2024). Detection of land cover usage from optimized learnable parameter artificial neural network (OLPANN) using multispectral images. *Multimedia Tools and Applications*. https://doi.org/10.1007/s11042-024-18828-2

Gröschler K C, Martens T, Schrautzer J & Oppelt N (2025). Data-driven identification of high-nature value grasslands using Harmonized Landsat Sentinel-2 time series data. *Remote Sensing Applications: Society and Environment* 37, 101427. https://doi.org/10.1016/J.RSASE.2024.101427

Guan, H, Li J, Chapman M, Deng F, Ji Z & Yang X (2013). Integration of orthoimagery and lidar data for object-based urban thematic mapping using random forests. *International Journal of Remote Sensing* 34(14): 5166–5186. https://doi.org/10.1080/01431161.2013.788261

Ha N T, Manley-Harris M, Pham T D & Hawes I (2020). A comparative assessment of ensemble-based machine learning and maximum likelihood methods for mapping seagrass using sentinel-2 imagery in Tauranga Harbor, New Zealand. *Remote Sensing* 12(3). https://doi.org/10.3390/rs12030355

Hasituya & Chen Z (2017). Mapping Plastic-Mulched Farmland with Multi-Temporal Landsat-8 Data. *Remote Sensing* 9(6). https://doi.org/10.3390/rs9060557

Hasituya H, Chen Z, Wang L, Wu W, Jiang Z & Li H (2016). Monitoring Plastic-Mulched Farmland by Landsat-8 OLI Imagery Using Spectral and Textural Features. *Remote Sensing* 8(4). https://doi.org/10.3390/rs8040353

Huang C, Davis L S & Townshend J R G (2002). An assessment of support vector machines for land cover classification. *International Journal of Remote Sensing* 23(4): 725–749. https://doi.org/10.1080/01431160110040323

Ibrahim E & Gobin A (2021). Sentinel-2 Recognition of Uncovered and Plastic Covered Agricultural Soil. *Remote Sensing* 13(21). https://doi.org/10.3390/rs13214195

Jiménez-Lao R, Aguilar F J, Nemmaoui A & Aguilar M A (2020). Remote sensing of agricultural greenhouses and plastic-mulched farmland: An analysis of worldwide research. *Remote Sensing* 12(16). https://doi.org/10.3390/RS12162649

Kalacska M, Lucanus O, Sousa L & Arroyo-Mora J P (2020). *High-Resolution Surface Water Classifications of the Xingu River, Brazil, Pre and Post Operationalization of the Belo Monte Hydropower Complex*. https://doi.org/10.6084/m9.figshare.12521900.v1

Koc-San D (2013). Evaluation of Different Classification Techniques for the Detection of Glass and Plastic Greenhouses from WorldView-2 Satellite Imagery. *Journal of Applied Remote Sensing* 7(1): 073553. https://doi.org/10.1117/1.jrs.7.073553

Koc-San D, San B T, Bakis V, Helvaci M & Eker Z (2013). Multi-Criteria Decision Analysis integrated with GIS and remote sensing for astronomical observatory site selection in Antalya province, Turkey. *Advances in Space Research* 52(1): 39–51. https://doi.org/10.1016/J.ASR.2013.03.001

Kpienbaareh D, Sun X, Wang J, Luginaah I, Kerr R B, Lupafya E & Dakishoni L (2021). Crop type and land cover mapping in northern malawi using the integration of sentinel-1, sentinel-2, and planetscope satellite data. *Remote Sensing* 13(4): 1–21. https://doi.org/10.3390/rs13040700

Lawrence R L, Wood S D & Sheley R L (2006). Mapping invasive plants using hyperspectral imagery and Breiman Cutler classifications (randomForest). *Remote Sensing of Environment* 100(3): 356–362. https://doi.org/10.1016/J.RSE.2005.10.014

Li J, Wang H, Wang J, Zhang J, Lan Y & Deng Y (2023). Combining Multi-Source Data and Feature Optimization for Plastic-Covered Greenhouse Extraction and Mapping Using the Google Earth Engine: A Case in Central Yunnan Province, China. *Remote Sensing* 15(13). https://doi.org/10.3390/rs15133287

Li X, Chen W, Cheng X & Wang L (2016). A comparison of machine learning algorithms for mapping of complex surface-mined and agricultural landscapes using ZiYuan-3 stereo satellite imagery. *Remote Sensing* 8(6). https://doi.org/10.3390/rs8060514

Liu C, Frazier P & Kumar L (2007). Comparative assessment of the measures of thematic classification accuracy. *Remote Sensing of Environment* 107(4): 606–616. https://doi.org/10.1016/J.RSE.2006.10.010

Loukika K N, Keesara V R & Sridhar V (2021). Analysis of land use and land cover using machine learning algorithms on google earth engine for Munneru river basin, India. *Sustainability (Switzerland)* 13(24). https://doi.org/10.3390/su132413758

Lu L, Di L & Ye Y (2014). A decision-tree classifier for extracting transparent plastic-mulched Landcover from landsat-5 TM images. *IEEE Journal of Selected Topics in Applied Earth Observations and Remote Sensing* 7(11): 4548–4558. https://doi.org/10.1109/JSTARS.2014.2327226

Maccioni A, Agati G & Mazzinghi P (2001). New vegetation indices for remote measurement of chlorophylls based on leaf directional reflectance spectra. *Journal of Photochemistry and Photobiology B: Biology* 61(1–2): 52–61. https://doi.org/10.1016/S1011-1344(01)00145-2

Malarvizhi K, Kumar S V & Porchelvan P (2016). Use of High Resolution Google Earth Satellite Imagery in Landuse Map Preparation for Urban Related Applications. *Procedia Technology* 24: 1835–1842. https://doi.org/10.1016/J.PROTCY.2016.05.231

Mallick K, Verfaillie J, Wang T, Ortiz A A, Szutu D, Yi K, Kang Y, Short, R, Hu T, Sulis M, Szantoi Z, Boulet G, Fisher J B & Baldocchi D (2024). Net fluxes of broadband shortwave and photosynthetically active radiation complement NDVI and near infrared reflectance of vegetation to explain gross photosynthesis variability across ecosystems and climate. *Remote Sensing of Environment* 307, 114123. https://doi.org/10.1016/J.RSE.2024.114123

Manos E, Witharana C, Udawalpola R, Hasan A & Liljedahl A K (2022). Convolutional Neural Networks for Automated Built Infrastructure Detection in the Arctic Using Sub-Meter Spatial Resolution Satellite Imagery. *Remote Sensing* 14(11). https://doi.org/10.3390/rs14112719

Mary R, Nasir R, Alam A, Tariq A, Nawaz R, Javied S, Zaman Q, Islam F & Nawaz Khan S (2023). Exploring hazard quotient, cancer risk, and health risks of toxic metals of the Mehmood Booti and Lakhodair landfill groundwaters, Pakistan. *Environmental Nanotechnology, Monitoring & Management* 20: 100838. https://doi.org/10.1016/J.ENMM.2023.100838

McBratney A, Field D J & Koch A (2014). The dimensions of soil security. *Geoderma* 213: 203–213. https://doi.org/10.1016/J.GEODERMA.2013.08.013

Millard K & Richardson M (2015). On the importance of training data sample selection in Random Forest image classification: A case study in peatland ecosystem mapping. *Remote Sensing* 7(7): 8489–8515. https://doi.org/10.3390/rs70708489

Mokhtari A, Sadeghi M, Afrasiabian Y & Yu K (2023). OPTRAM-ET: A novel approach to remote sensing of actual evapotranspiration applied to Sentinel-2 and Landsat-8 observations. *Remote Sensing of Environment* 286: 113443. https://doi.org/10.1016/J.RSE.2022.113443

Myint S W, Gober P, Brazel A, Grossman-Clarke S & Weng Q (2011). Per-pixel vs. object-based classification of urban land cover extraction using high spatial resolution imagery. *Remote Sensing of Environment* 115(5): 1145–1161. https://doi.org/10.1016/J.RSE.2010.12.017

Nemmaoui A, Aguilar M A, Aguilar F J, Novelli A & Lorca A G (2018). Greenhouse crop identification from multi-temporal multi-sensor satellite imagery using object-based approach: A case study from Almería (Spain). *Remote Sensing* 10(11). https://doi.org/10.3390/rs10111751

Novelli A, Aguilar M A, Nemmaoui A, Aguilar F J & Tarantino E (2016). Performance evaluation of object based greenhouse detection from Sentinel-2 MSI and Landsat 8 OLI data: A case study from Almería (Spain). *International Journal of Applied Earth Observation and Geoinformation* 52: 403–411. https://doi.org/10.1016/j.jag.2016.07.011

Novelli A & Tarantino E (2015). Combining Ad Hoc Spectral İndices Based on Landsat-8 OLI/TIRS Sensor Data for the Detection of Plastic Cover Vineyard. *Remote Sensing Letters* 6(12): 933–941. https://doi.org/10.1080/2150704X.2015.1093186

Ou C, Yang J, Du Z, Liu Y, Feng Q & Zhu D (2020). Long-Term Mapping of a Greenhouse in a Typical Protected Agricultural Region Using Landsat Imagery and the Google Earth Engine. *Remote Sensing* 12(1): 55. https://doi.org/10.3390/rs12010055

Ouma Y, Nkwae B, Moalafhi D, Odirile P, Parida B, Anderson G & Qi J (2022). Comparison of Machine Learning Classifiers for Multitemporal and Multisensor Mapping of Urban LULC Features. *International Archives of the Photogrammetry, Remote Sensing and Spatial Information Sciences - ISPRS Archives* 43: 681–689. https://doi.org/10.5194/isprs-archives-XLIII-B3-2022-681-2022

Pal M (2005). Random forest classifier for remote sensing classification. *International Journal of Remote Sensing* 26(1): 217–222. https://doi.org/10.1080/01431160412331269698

Pal M & Foody G M (2012). Evaluation of SVM, RVM and SMLR for accurate image classification with limited ground data. *IEEE Journal of Selected Topics in Applied Earth Observations and Remote Sensing* 5(5): 1344–1355. https://doi.org/10.1109/JSTARS.2012.2215310

Pan Y, Qin J, Hou Y & Chen J J (2024). Two-stage support vector machine-enabled deep excavation settlement prediction considering class imbalance and multi-source uncertainties. *Reliability Engineering & System Safety* 241: 109578. https://doi.org/10.1016/J.RESS.2023.109578

Patela N N, Angiul, E, Gamba P, Gaughan A, Lisini G, Stevens F R, Tatem A J & Trianni G (2015). Multitemporal settlement and population mapping from Landsat using Google Earth Engine. *International Journal of Applied Earth Observation and Geoinformation* 35: 199–208. https://doi.org/10.1016/J.JAG.2014.09.005

Pelletier C, Valero S, Inglada J, Champion N, Sicre C M & Dedieu G (2017). Effect of training class label noise on classification performances for land cover mapping with satellite image time series. *Remote Sensing* 9(2). https://doi.org/10.3390/rs9020173

Perilla G A & Mas J F (2019). High-Resolution Mapping of Protected Agriculture in Mexico, Through Remote Sensing Data Cloud Geoprocessing. *European Journal of Remote Sensing* 52(1): 532–541. https://doi.org/10.1080/22797254.2019.1686430

Phinzi K, Ngetar N S, Pham Q B, Chakilu G G & Szabó S (2023). Understanding the role of training sample size in the uncertainty of high-resolution LULC mapping using random forest. *Earth Science Informatics* 16(4): 3667–3677. https://doi.org/10.1007/s12145-023-01117-1

Piramuthu S (2008). Input data for decision trees. *Expert Systems with Applications*, 34(2): 1220–1226. https://doi.org/10.1016/J.ESWA.2006.12.030

Prasad A M, Iverson L R & Liaw A (2006). Newer classification and regression tree techniques: Bagging and random forests for ecological prediction. *Ecosystems* 9(2): 181–199. https://doi.org/10.1007/s10021-005-0054-1

Qu Y & Long H (2018). The economic and environmental effects of land use transitions under rapid urbanization and the implications for land use management. *Habitat International* 82: 113–121. https://doi.org/10.1016/J.HABITATINT.2018.10.009

Rodriguez-Galiano V F, Ghimire B, Rogan J, Chica-Olmo M & Rigol-Sanchez J P (2012). An assessment of the effectiveness of a random forest classifier for land-cover classification. *ISPRS Journal of Photogrammetry and Remote Sensing*, 67(1): 93–104. https://doi.org/10.1016/J.ISPRSJPRS.2011.11.002

Rouse J W, Haas R H, Schell J A & Deering D W (1974). Monitoring vegetation systems in the Great Plains with ERTS. *NASA Spec. Publ* 351(1): 309.

Salas E A L & Henebry G M (2012). Separability of maize and soybean in the spectral regions of chlorophyll and carotenoids using the Moment Distance Index. *Israel Journal of Plant Sciences* 60(1–2): 65–76. https://doi.org/10.1560/IJPS.60.1-2.65

Srivastava P K, Han D, Rico-Ramirez M A, Bray M & Islam T (2012). Selection of classification techniques for land use/land cover change investigation. *Advances in Space Research* 50(9): 1250–1265. https://doi.org/10.1016/J.ASR.2012.06.032

Stehfest E, Van Zeist W J, Valin H, Havlik P, Popp A, Kyle P, Tabeau A, Mason-D'Croz D, Hasegawa T, Bodirsky B L, Calvin, K, Doelman J C, Fujimori S, Humpenöder F, Lotze-Campen H, Van Meijl H & Wiebe K (2019). Key determinants of global land-use projections. *Nature Communications* 10(1). https://doi.org/10.1038/s41467-019-09945-w

Stoian A, Poulain V, Inglada J, Poughon V & Derksen D (2019). Land cover maps production with high resolution satellite image time series and convolutional neural networks: Adaptations and limits for operational systems. *Remote Sensing* 11(17). https://doi.org/10.3390/rs11171986

Sun X, Li X, Tan B, Gao J, Wang L & Xiong S (2025). Integrating Otsu Thresholding and Random Forest for Land Use/Land Cover (LULC) Classification and Seasonal Analysis of Water and Snow/Ice. *Remote Sensing* 17(5). https://doi.org/10.3390/rs17050797

Talukdar S, Singha P, Shahfahad Mahato S, Praveen B & Rahman A (2020). Dynamics of ecosystem services (ESs) in response to land use land cover (LU/LC) changes in the lower Gangetic plain of India. *Ecological Indicators 112*: 106121. https://doi.org/10.1016/J.ECOLIND.2020.106121

Tariq A, Jiango Y, Li Q, Gao J, Lu L, Soufan W, Almutairi K F & Habib-ur-Rahman M (2023). Modelling, mapping and monitoring of forest cover changes, using support vector machine, kernel logistic regression and naive bayes tree models with optical remote sensing data. *Heliyon* 9(2). https://doi.org/10.1016/J.HELIYON.2023.E13212

Vapnik V (2013). *The nature of statistical learning theory*. Springer science & business media.

Veettil B K, Van D D, Quang N X & Hoai P N (2022). Remote Sensing of Plastic-Covered Greenhouses and Plastic-Mulched Farmlands: Current Trends and Future Perspectives. In *Land Degradation and Development*. John Wiley and Sons Ltd. https://doi.org/10.1002/ldr.4497

Veettil B K & Xuan Q N (2022). Correction to: Landsat-8 and Sentinel-2 Data for Mapping Plastic-Covered Greenhouse Farming Areas: A Study From Dalat City (Lam Dong Province), Vietnam. In *Environmental Science and Pollution Research* 29 (49): 73934. Springer Science and Business Media Deutschland GmbH. https://doi.org/10.1007/s11356-022-21677-x

Xie Z, Chen Y, Lu D, Li G & Chen E (2019). Classification of land cover, forest, and tree species classes with Ziyuan-3 multispectral and stereo data. *Remote Sensing* 11(2). https://doi.org/10.3390/rs11020164

Xiong Y, Zhang Q, Chen X, Bao A, Zhang J & Wang Y (2019). Large Scale Agricultural Plastic Mulch Detecting and Monitoring with Multi-Source Remote Sensing Data: A Case Study in Xinjiang, China. *Remote Sensing* 11(18). https://doi.org/10.3390/rs11182088

Xue J & Su B (2017). Significant remote sensing vegetation indices: A review of developments and applications. In *Journal of Sensors* 2017. https://doi.org/10.1155/2017/1353691

Yang D, Chen J, Zhou Y, Chen X, Chen X & Cao X (2017). Mapping plastic greenhouse with medium spatial resolution satellite data: Development of a new spectral index. *ISPRS Journal of Photogrammetry and Remote Sensing*, 128, 47–60. https://doi.org/10.1016/J.ISPRSJPRS.2017.03.002

Yang D, Sun S, Chen J & Liu X (2016). Analysis for the spatial and temporal patterns of plasticulture In Shandong Province, China with remotely sensed data. *2016 Fifth International Conference on Agro-Geoinformatics (Agro-Geoinformatics)* 1–4.

Yilmaz O S, Ateş A M & Gülgen F (2023). A novel approach suggestion for assessing the impact of topographic shading on the estimation of the floating photovoltaic technical potential. *Energy* 283: 128479. https://doi.org/10.1016/j.energy.2023.128479

Zarco-Tejada P J, González-Dugo V & Berni J A J (2012). Fluorescence, temperature and narrow-band indices acquired from a UAV platform for water stress detection using a micro-hyperspectral imager and a thermal camera. *Remote Sensing of Environment* 117: 322–337. https://doi.org/10.1016/J.RSE.2011.10.007

Zhang T, Tang B H, Huang L & Chen G (2022). Rice and Greenhouse Identification in Plateau Areas Incorporating Sentinel-1/2 Optical and Radar Remote Sensing Data from Google Earth Engine. *Remote Sensing* 14(22). https://doi.org/10.3390/rs14225727

Zhao GengXing Z G, Li Jing L J, Li Tao L T, Yue YuDe Y Y & Warner T (2004). *Utilizing landsat TM imagery to map greenhouses in Qingzhou, Shandong Province, China.*

Zhao M, Xue B, Li B, Zhu J & Song W (2024). Ensemble learning with support vector machines algorithm for surface roughness prediction in longitudinal vibratory ultrasound-assisted grinding. *Precision Engineering* 88: 382–400. https://doi.org/10.1016/J.PRECISIONENG.2024.02.018

Zhao Z, Islam F, Waseem L A, Tariq A, Nawaz M, Islam I U, Bibi T, Rehman N U, Ahmad W, Aslam R W, Raza D & Hatamleh W A (2024). Comparison of Three Machine Learning Algorithms Using Google Earth Engine for Land Use Land Cover Classification. *Rangeland Ecology & Management* 92: 129–137. https://doi.org/10.1016/j.rama.2023.10.007

Zhu Y, Geis C, So E & Jin Y (2021). Multitemporal Relearning with Convolutional LSTM Models for Land Use Classification. *IEEE Journal of Selected Topics in Applied Earth Observations and Remote Sensing* 14: 3251–3265. https://doi.org/10.1109/JSTARS.2021.3055784

Copyright © 2026 The Author(s). This is an open-access article published by Faculty of Agriculture, Ankara University under the terms of the Creative Commons Attribution License which permits unrestricted use, distribution, and reproduction in any medium or format, provided the original work is properly cited.